Solid Earth Discuss., 7, 2807–2831, 2015
www.solid-earth-discuss.net/7/2807/2015/
doi:10.5194/sed-7-2807-2015

Solid Earth Discussions
Open Access

X-ray microtomography analysis of soil structure deformation caused by centrifugation

S. Schlüter[1,2], **F. Leuther**[1], **S. Vogler**[2], **and H.-J. Vogel**[1,3]

[1]Helmholtz-Zentrum für Umweltforschung GmbH – UFZ, Halle (Saale), Germany
[2]Deutsches Zentrum für Neurodegenerative Erkrankungen – DZNE, Dresden, Germany
[3]Martin-Luther-Universität Halle-Wittenberg, Halle (Saale), Germany

Received: 2 September 2015 – Accepted: 15 September 2015 – Published: 6 October 2015

Correspondence to: S. Schlüter (steffen.schlueter@ufz.de)

Published by Copernicus Publications on behalf of the European Geosciences Union.

Abstract

Centrifugation provides a fast method to measure soil water retention curves over a wide moisture range. However, deformation of soil structure may occur at high rotation speed in the centrifuge. These changes in soil structure were analyzed with X-ray microtomography. A detailed analysis of the pore space reveals an interplay between shrinkage due to drying and soil compaction due to compression. While volume changes due to swelling clay minerals are immanent to any drying process, the compaction of soil is a specific drawback of the centrifugation method. A new protocol for digital volume correlation was developed to analyze the spatial heterogeneity of deformation. The displacement of soil constituents is highest in the top part of the sample and exhibits high lateral variability explained by the spatial distribution of macropores in the sample. Centrifugation should therefore only be applied after the completion all other hydraulic or thermal experiments, or any other analysis that depends on the integrity of soil structure.

1 Introduction

Soils, rocks and sediments are assumed to be rigid bodies in many modelling applications. Yet, the internal structure of these porous media is modified through a variety of technical and natural processes. The internal changes can either be gradual, e.g. through dissolution, biological activity or swelling/shrinking, or abrupt, e.g. landslides or tillage. Coventional laboratory methods can only provide a limited set of structural properties like bulk density and porosity or provide indirect information through functional properties that are governed by the internal structure like gas diffusion, permeability or stress–strain relationships. Direct information on the deformation of the internal pore architecture is typically missing. X-ray microtomography has turned into a standard technique to fill this gap and measure the three-dimensional internal structure of porous media (Ketcham and Carlson, 2001; Cnudde and Boone, 2013; Wildenschild

SED
7, 2807–2831, 2015

and Sheppard, 2013). There is a huge variety of image processing and image analysis methods that are all tailored for the ultimate goal to quantify the complex, structural heterogeneity based on a few meaningful parameters (Kaestner et al., 2008; Vogel et al., 2010; Schlüter et al., 2014). The changes in the internal structure can be assessed statistically, e.g. by comparing the pore size distribution or pore connectivity averaged over different samples at two points in time (Jégou et al., 2002; Schlüter et al., 2011). Evidently, spatially explicit information about the internal displacement of particles or aggregates is excluded from analysis in such an approach. However, this local deformation information is of particular interest, e.g. in soil mechanics (Terzaghi et al., 1996). So far there are only a few approaches to measure the deformation explicitly via imaging and image analysis. One method would obviously be to manually identify identical objects in two consecutive images and measure their separation distance. Repeating this measurement for many objects would then populate the deformation field. However, this is impractical for large, three-dimensional datasets, because of the large number of measurements required to reach an appropriate density of displacement information. Therefore, automatic methods are needed.

These automated methods are usually based on digital volume correlation (Bay et al., 1999; Lenoir et al., 2007; Peth et al., 2010; Hall, 2010; Son et al., 2012). The rationale of this method is to recover the displacement field by finding a geometric transformation of a deformed image that optimizes a correlation coefficient with the original, undeformed target image. The method usually comprises three steps (Bay et al., 1999): (1) the acquisition of X-ray microtomaphy image before and after the pertubation, (2) image registration of one image onto the other to obtain a discrete deformation vector field and (3) calculation of the strain tensor field from the displacement vector field. Another popular method for change detection is called particle image velocimetry (PIV) (White, 2003). PIV was originally developed to visualize flow paths within a fluid by tracking small, yet visible particles over time (Adrian, 1991). In this method the image is divided into a large number of sub-windows, and the displacement vector for each window is calculated via cross-correlation between two consecutive images, which results in a local

SED
7, 2807–2831, 2015

velocity for the given time lag. The particles can be substituted by any moving feature such as a growing root (Bengough et al., 2010), soil displacement along an earthworm borrough (Barnett et al., 2009) or soil creeping along slopes (Baba and Peth, 2012). A serious shortcoming of PIV is that so far it can only be applied to two-dimensional sections, in which case any displacement out of plane into the third dimension is excluded.

The objective of this paper is to measure local deformations in a soil core during centrifugation with digital volume correlation. We put special emphasis on common pitfalls and best practices for image registration, which is the critical step for a successful application of this method.

Measuring the water loss through centrifugation of a soil is a rather old method for determining the water retention curve of a soil (Gardner, 1937; Russell and Richards, 1939; Oden, 1975; Reatto et al., 2008). It has obvious advantages over other conventional methods like multi-step outflow (Van Dam et al., 1994; Vogel and Ippisch, 2008) or evaporation (Simunek et al., 1998; Peters and Durner, 2008) in that the method is less time consuming, it captures a wide moisture range of the retention curve and provides a good reproducibility through defined experimental conditions (angular velocity, temperature, pressure). More recently, the steady state centrifugation method was also used to measure the unsaturated hydraulic conductivity of soils (Šimůnek and Nimmo, 2005; Van den Berg et al., 2009). However, a serious drawback is that soil can get compacted through the centrifugal force, i.e. the inertia that acts on the sample during rotation (Khanzode et al., 2002; Wedler and Boguslawski, 1965). The motivation for this study is therefore to scrutinize the assumption of a rigid soil matrix in order to assess the suitability of centrifugation for measuring water retention in soil.

2 Background

Since image registration is the backbone of our deformation detection method, we provide a brief overview over the core concepts. The spatial alignment of a altered image

SED
7, 2807–2831, 2015

with a target image is usually achieved by minimizing an objective function that quantifies the mismatch in terms of a predefined metric. A standard metric would be the correlation coefficient between co-localized voxels (Latham et al., 2008; Hapca et al., 2011). More advanced metrices are based on information theory like mutual information criteria (Mattes et al., 2001). Composite metrics are also possible, e.g. with an additional regularization term in case of non-rigid registration or an additional term for the mismatch of manually defined point pairs, so-called landmarks. The geometrical transform that produces an optimized alignment can be grouped according to the degrees of freedom by which the image can move. The simplest transform is rigid registration with six degrees of freedom, i.e. rotation around three axes and translation in three directions. A similarity transform includes isotropic scaling as one additional parameter. Affine transformations possess twelve degrees of freedom through rotation, translation, shearing in three directions and anisotropic scaling. All aforementioned transforms are global in that a single transformation matrix is uniformly applied to the entire image. Thus they do not allow for deformation. Elastic registration with a B-Spline transform, in turn, requires a regular grid of control points over the image where each performs independent, affine registrations. As a consequence, the control points move relative to each other in the course of registration. Image registration is achieved by an iterative optimization scheme with standard methods like gradient descent or more involved methods like adaptive stochastic gradient descent (Klein et al., 2010) with optimal trade-off between speed and robustness. This completes the description of the core methodology of automated image registration. However, a straightforward implementation will most certainly lead to a failure of the method without following some best practices:

1. Initialization: salient objects in the altered and the target image need to have substantial overlap to identify a meaningful correspondence of features. This is facilitated by a manually edited transformation matrix, in which the resolution of the altered image is adapted to the resolution of the target image and an offset between the images is corrected by some initial translation or rotation of the altered

SED
7, 2807–2831, 2015

image. This manual procedure can be avoided by exhaustive sampling, where all combinations of translations (and rotations if required) are tested at a coarse grid representation (Latham et al., 2008). A different kind of user input is provided by landmarks placed on the salient features in both images. The cumulative Euclidean distance between point pairs is then added as a second term to the objective function. In all cases, the correct orientation of the sample has to be ensured a priori, because a flipped orientation cannot be recovered by rotation.

2. Concatenation: it is often useful to combine several consecutive image registration steps with each other, especially when an elastic registration with thousands of degrees of freedom is involved. Then a rigid registration can place the altered image already close to the global minimum and thus anticipate a collective movement of all control points in the subsequent B-Spline transform. In our example, a two-step procedure will first match the position of the fixed core holder in the original sample with that of deformed sample after centrifugation, by aligning corresponding landmarks on the core wall. Then, a B-Spline Transform of the centrifuged sample onto the original sample will only recover the remaining internal deformations.

3. Pyramid schedule: as mentioned above, a coarse representation of both images at reduced resolution vastly reduces the processing time so that it may even allow for exhaustive sampling of all transform parameter combinations. At the same time the coarsening reduces the iterations necessary to achieve a certain translation in physical space. This can be achieved with a so-called pyramid schedule. That is, the registration is started at a coarse representation and when convergence is reached the registration is continued at the next pyramid level with higher resolution. Finer details, e.g. small rocks, that did not appear at a coarse level are used then to refine the registration results.

SED
7, 2807–2831, 2015

3 Materials and methods

3.1 Soil sampling

Undisturbed soil was sampled from the upper soil layer (5 to 15 cm) of a grass land soil near Halle/Saale, Germany, using a custom-made drill for undisturbed sampling of cylindrical soil cores (UGT GmbH, Germany). The samples were covered with a lid, carefully transported to the laboratory and stored in a fridge at 4 °C to prevent the soil from drying and to reduce the biological activity. The soil sample had a mean height of 7.9 cm, a diameter of 9.4 cm and an initial bulk density of 1.24 g cm^{-3}. The texture of the soil was composed of 24 % sand, 58 % silt and 18 % clay (disregarding organic matter and rocks > 2 mm in diameter).

3.2 Centrifugation

The experimental determination of soil water retention curves via centrifugation is achieved through weighting of excess water drained from the sample at a certain angular velocity. A perforated metal plate covered with a filter paper (pore size 10 µm) was installed in between the lower boundary of the sample and a reservoir that collects the drained water. This setup was placed in a centrifuge (Cryofuge 6000i, Heraeus GmbH, Germany) and covered with a plastic film to prevent evaporation. The capillary pressure was initially adjusted to full saturation. Afterwards, the sample was centrifuged at increasing angular velocities and each step was kept constant long enough until no more water is released. The equivalent capillary pressure of water ψ in equilibrium with the gravitational field written in differential form is (Gardner, 1937; Russell and Richards, 1939):

$$\frac{\partial \psi}{\partial r} = \rho \omega^2 r. \quad (1)$$

SED
7, 2807–2831, 2015

Integrating Eq. (1) between the inner (r_i = 0.136 m) and outer (r_o = 0.22 m) boundaries of the soil core one obtains

$$\psi = \frac{\rho\omega^2}{2}(r_o^2 - r_i^2), \quad (2)$$

where normalizing by the density of water ρ results in work per unit mass of water and hence pressure [Pa]. The angular velocity ω was calculated by $\omega = 2\pi \cdot N$, where N is the revolution frequency [rad s^{-1}]. After each centrifugation step we recorded the weight of the sample. Note that ψ scales quadratically with radius, while the change in local water content may be much larger due to the non-linearity of the water retention curve. So averaging over a tall sample can lead to an internal gradient in water content and an apparent reduction of the steepness in the water retention curve. In the end, the sample was oven-dried for 2 days at 105 °C to determine the dry weight and total water content.

3.3 X-Ray microtomography

The soil cores were scanned with an X-ray microtomograph (X-TEk XCT 225, Nikon Metrology) at an energy of 150 keV and a beam current of 425 µA, resulting in a power of 63.8 W. Additionally, we used a 1 mm copper filter to reduce beam hardening artifacts. An entire scan comprised 2749 projections with an exposure time of 708 ms. The reconstruction of three-dimensonal images was done with the CT Pro 3-D software package (version 3.1) at a spatial resolution of 60 µm.

3.4 Image registration

Image registration was carried out with *elastix*[1] (Klein et al., 2010), an open-source image registration tool based on *ITK* (Ibanez et al., 2005) which was tailored for medical imaging applications. Raw images were scaled by a factor of three to a resolution of

[1] http://elastix.isi.uu.nl

SED
7, 2807–2831, 2015

180 µm in order to reduce memory consumption. The image of the original soil structure was registered to the deformed soil in two steps. First, we applied a rigid registration that optimizes the mutual information criterion between both images (Mattes et al., 2001). The outcome of such a registration would be a compromise between alignment with the rigid wall and the deformed interior. Therefore we added landmarks at four notches in the wall and add the Euclidean distance between corresponding landmarks as an additional metric.

After the sample walls were perfectly aligned, we applied elastic registration with a B-Spline transform to recover internal deformations. Here, the additional problem took effect that macropores are not rigid and may disappear completely. However, a lack of corresponding features impairs the success of image registration. To avoid this, we rescaled the histogram of the images such that pore and soil matrix voxels have zero gray value and all rigid rocks are depicted with optimal contrast. The local displacement of rocks then constitutes the deformation field. A regularization term, called bending energy, was added to the objective function which ascertains that local transitions in deformation magnitude and direction are smooth (Klein et al., 2010).

Two sample images and all parameter files to reproduce the entire workflow are available from the authors upon request.

3.5 Image analysis

The deformation results are complemented by quantitative image analysis of the changes in the macropore structure due to centrifugation. To do so, the raw images were denoised with a non-local means filter implemented in ITK (Buades et al., 2005; Tristán-Vega et al., 2012). Subsequently, automatic threshold detection for three classes (pores, soil matrix, rocks) was achieved with fuzzy c-means analysis of the histogram (Jawahar et al., 1997; Schlüter et al., 2014) and segmentation was carried out with simple thresholding. The resulting pore space was analyzed towards two different directions. First, pore size distributions were calculated with the maximum inscribed sphere method using the BoneJ plugin (version 1.3.12) in Fiji (Doube et al., 2010). Sec-

SED
7, 2807–2831, 2015

ond, depth profiles of porosity were computed in equidistant steps of 600 µm to monitor the depth dependent changes of macroporosity caused by drying and compaction. All image processing steps except denoising and pore size analysis were performed with the QuantIm image processing library (Vogel et al., 2010; Schlüter et al., 2014).

4 Results

4.1 Centrifugation

The water release through an iterative increase in angular velocity of the centrifuge is depicted in Fig. 1. Angular velocity ω is converted into capillary pressure ψ with Eq. (2) in order to obtain a soil water retention curve in conventional units. A van Genuchten parametrization was fitted to the data, which has the following form (van Genuchten, 1980):

$$\theta(\psi) = \theta_r + \frac{\theta_s - \theta_r}{[1 + [\alpha|\psi|]^n]^{1-1/n}}, \quad (3)$$

where θ_s is saturated water content, θ_r is residual water content and α and n are empirical parameters that relate to the air-entry point and the steepness of the curve. The resulting parameter set ($\alpha = 0.23\,\mathrm{kPa}^{-1}$, $n = 1.22$, $\theta_s = 0.47$, $\theta_r = 0.16$) was achieved with a very high coefficient of determination ($R^2 = 0.999$). Although the measured data can be perfectly described by the model this does not allow for any inference about the structural changes within the sample. Since internal deformation through centrifugation is supposed to be highest for the highest accelaration rates in the centrifuge, the sample was scanned with X-ray microtomography at a capillary pressure of $\psi = -100\,\mathrm{kPa}$ and $\psi = -500\,\mathrm{kPa}$, as well as at full saturation ($\psi = 0\,\mathrm{kPa}$) to provide an undisturbed reference.

SED
7, 2807–2831, 2015

4.2 X-ray microtomography

The 3-D structure of the sample at full water saturation is depicted in Fig. 2a. Rocks of different sizes are embedded in a loamy soil matrix and large macropores are present in all depths. After centrifugation down to a capillary pressure of $\psi = -100$ kPa the structure is markedly deteriorated Fig. 2b. The shape and positition of macropores have changed and dessication cracks have formed in the vicinity of macropores. A perforated, rigid plate is visible, which was mounted at the bottom of the sample to prevent soil loss during centrifugation and transport. At a capillary pressure of $\psi = -500$ kPa the soil is severly compacted as can been seen by the larger head space above the soil surface (Fig. 2c). Macropores are almost absent especially in the lower part of the sample and only a few dessication cracks with vertical orientation remain in the upper part of the profile.

These visual observations are corroborated by quantitative analysis of the pore space (Fig. 3). Macropores > 1 mm in diameter are less abundant in the soil at $\psi = -100$ kPa as compared to the reference at full water saturation, whereas macropores in the range of 0.1–1 mm are more frequent. This is because (1) bigger macropores shrunk into this size range and (2) new desiccation cracks due to soil drying mainly formed in that size range. The subsequent centrifugation to a capillary pressure of $\psi = -500$ kPa removed porosity in all size ranges.

The change in porosity through centrifugation is not evenly distributed across the sample (Fig. 4). Dessication cracks at $\psi = -100$ kPa mainly formed in the top part of the sample, whereas the bottom part of the sample exhibits lower porosity than the reference sample due to compaction. The sample in its driest state is compacted across the entire profile. The decline in macroporosity increases with depth. Evidently this is because the inertial force that acts on the soil in a given depth, i.e. $F_z = m\omega^2 r$, increases both with increasing overburden m and increasing absolute accelaration (due to $r_o > r_i$). A specific rock close to the soil surface served as a cut-off height for the profile. Its position changed from 68 to 58 and to 55 mm, respectively. The reduction

SED
7, 2807–2831, 2015

in total porosity due to the compaction normal to the rotation axis is in contrast to the increase in visible macroporosity from 10.9 to 12.3 % for $\psi = -100$ kPa, followed by 6.2 % for $\psi = -500$ kPa.

In summary, the pore space analysis is especially suited to identify changes in macroporosity due to crack formation and compression. The range of pore diameters that can be depicted with X-ray microtomography is rather small (> 60 µm) and limited by image resolution. Information about sub-voxel changes in porosity is lost. Furthermore, inference about internal deformation in the sample is not possible. The only information about the degree of deformation provided so far is a reduction in sample height, which could easily be achieved without 3-D imaging. In the following, we will demonstrate the power of digital image correlation to provide detailed information about internal deformation in soil.

4.3 Deformation

Rocks are especially suited to track internal deformations as they change in position, but not in shape. The poor spatial alignment of rocks between the saturated (green) and the centrifuged soil at a capillary pressure of $\psi = -500$ kPa (red) after the Euler transform is depicted in Fig. 5a. Evidently, the mismatch is highest for rocks close to the soil surface and smallest for rocks close to the bottom. Elastic registration with a B-Spline transform leads to a very good spatial alignment of rocks in all soil depths (Fig. 5b). Note that small rocks, e.g. within the black frames, have higher chance of registration failure due to the employed pyramid schedule. That is, large displacements vectors are retrieved at the coarse level, at which small rocks are averaged out. These rocks are well resolved at finer scales. However, if the same rock does not have a spatial overlap to begin with, then a first-order optimization algorithm like adaptive stochastic gradient descent cannot find a useful displacement vector.

An important result of the registration procedure is the displacement vector field (Fig. 6). There is a clear trend towards a downward movement of soil constituents as a consequence of compaction and its magnitude increases from $\psi = -100$ kPa to

SED
7, 2807–2831, 2015

$\psi = -500$ kPa. However, the direction and length of local displacement does not only vary with depth but also laterally. Furthermore, there is a substantial horizontal component of displacement in many locations. This lateral movement can have two different origins. First, the formation of mainly vertically aligned cracks displaces the soil normal to the crack but not along it. Secondly, regions of high macroporosity are preferential failure zones during compaction. Filling these macropores during compression with soil material from above evokes a lateral displacement component, because they are not evenly distributed across the soil.

5 Discussion

5.1 Pore scale processes during centrifugation

The analysis of macroporosity at µm resolution revealed substantial alterations of the pore space architecture during centrifugation. Without such a detailed X-ray microtomography analysis the only measurable, macroscopic changes in soil structure would have been an increase bulk density and a decrease in sample height. The conventional, quantitative image analysis of the pore space revealed a depth-dependent increase or decrease of macroporosity that resulted from the interplay of soil shrinkage due to drying and soil compaction due to compression. The deformation of the soil due to shrinkage is immanent to any drying process in presence of swelling clay minerals. So it would have also occured if drying is forced by another process, e.g. by evaporation. The compaction of the soil through centrifugal forces, however, is truely caused by the centrifugation process and represents a severe drawback of the method. A significant breakdown of structure through centrifugation was previously reported for an equivalent capillary pressure of $\psi = -100$ kPa (Wedler and Boguslawski, 1965) using a loess soil (5.4 % sand, 76,6 % silt, 18 % clay) that was less sandy than ours. Though this critical threshold is certainly substrate-dependent it compares well with the critical value found in this study. Furthermore, the soil sample in our current study was certainly

SED
7, 2807–2831, 2015

prone to soil compaction, because the initial bulk density was quite low (1.24 g cm^{-3}). If bulk density and thus mechanical stability was higher, then the susceptibility to soil compression is expected to be lower.

The question is, how this structure deformation ultimatively changes the measured water retention curve. Presumably, those macropores with the lowest mechanical stability are also the pores that drain first. That is, they have released their water, before they got deformed. Moreover, soil compaction leads to a general shift of the pore size distribution, during which the absolute abundance of smaller pores grows on the expense of bigger pores (Leij et al., 2002; Assouline, 2006). This effect causes an overestimation of water retention at lower (more negative) capillary pressures.

As a general advice, centrifugation should not be used to measure water retention curves down to very low pressure ranges if the sample is prone to soil compaction. For practical purposes the reduction in sample volume can be used as a suitable indicator to identify the critical pressure beyond which deformation has to be expected. If this method still has to be applied beyond this critical point, it should be performed at the end of all envisaged hydraulic or thermal experiments, as it causes irreversible damages to the internal soil structure.

5.2 Methodological limitations

We have developed a workflow for the automatic detection of soil structure deformation by means of free image registration software and outlined best practices in order to optimize the registration results both in terms of computational costs and accuracy. A major improvement for detecting the true deformation field was to use rocks for elastic registration. They change position and orientation, but in contrast to macropores they do not change their shape. As a consequence, they are more easily recovered by the spatial alignment process. The failure to recover the original position of some small rocks during elastic registration (black frame in Fig. 5) turns out to be a fundamental problem. If the displacement of small features relative to its surroundings is bigger

SED
7, 2807–2831, 2015

than the actual size of the feature, then it is very unlikely that the original position will be found. Only additional landmarks can help to improve the registration result in that case.

A general lack of rocks or other salient, rigid features may render elastic registration useless depending on the severity of deformation. In turn, if the focus is not on natural soil, but on technical substrates, then the addition of easily trackable features like rocks or metal particles is an easy way to improve the accurate detection of internal deformation.

6 Conclusions

Measuring the water release through soil centrifugation is a fast method to obtain soil water retention curves. Using X-ray microtomography we have corroborated previous findings that the soil structure starts to deteriorate at a capillary pressure of $\psi = -100$ kPa. Moreover, quantative analysis of the pore space at µm resolution revealed that the soil deformation is caused by the interplay of shrinkage and compaction. Local deformation was detected by a novel workflow for digital volume correlation based on elastic image registration. This method enables a detailed look at local soil deformation and its spatial variability. We applied this method to the measure changes in soil structure during centrifugation, however, this method has the potential to quantify the detailed mechanical deformation of soil and other materials exposed to any other type of external forcing.

Acknowledgements. This research was supported by the German Federal Ministry of Food and Agriculture (BMEL), award T343D123.

The article processing charges for this open-access publication were covered by a Research Centre of the Helmholtz Association.

References

Adrian, R. J.: Particle-imaging techniques for experimental fluid mechanics, Annu. Rev. Fluid Mech., 23, 261–304, 1991. 2809

Assouline, S.: Modeling the relationship between soil bulk density and the water retention curve, Vadose Zone J., 5, 554–563, doi:10.2136/vzj2005.0083, 2006. 2820

Baba, H. O. and Peth, S.: Large scale soil box test to investigate soil deformation and creep movement on slopes by Particle Image Velocimetry (PIV), Soil Till. Res., 125, 38–43, doi:10.1016/j.still.2012.05.021, 2012. 2810

Barnett, C., Bengough, A., and McKenzie, B.: Quantitative image analysis of earthworm-mediated soil displacement, Biol. Fert. Soils, 45, 821–828, doi:10.1007/s00374-009-0392-9, 2009. 2810

Bay, B., Smith, T., Fyhrie, D., and Saad, M.: Digital volume correlation: Three-dimensional strain mapping using X-ray tomography, Exp. Mech., 39, 217–226, doi:10.1007/BF02323555, 1999. 2809

Bengough, A. G., Hans, J., Bransby, M. F., and Valentine, T. A.: PIV as a method for quantifying root cell growth and particle displacement in confocal images, Microsc. Res. Techniq., 73, 27–36, doi:10.1002/jemt.20749, 2010. 2810

Buades, A., Coll, B., and Morel, J. M.: A non-local algorithm for image denoising, in: IEEE Computer Society Conference on Computer Vision and Pattern Recognition, 2005, CVPR 2005, San Diego, CA, USA, 20–25 June 2005 , vol. 2, 60–65, doi:10.1109/CVPR.2005.38, 2005. 2815

Cnudde, V. and Boone, M.: High-resolution X-ray computed tomography in geosciences: a review of the current technology and applications, Earth-Sci. Rev., 123, 1–17, doi:10.1016/j.earscirev.2013.04.003, 2013. 2808

Doube, M., Kłosowski, M. M., Arganda-Carreras, I., Cordelières, F. P., Dougherty, R. P., Jackson, J. S., Schmid, B., Hutchinson, J. R., and Shefelbine, S. J.: BoneJ: free and extensible bone image analysis in ImageJ, Bone, 47, 1076–1079, doi:10.1016/j.bone.2010.08.023, 2010. 2815

Gardner, R.: A method of measuring the capillary tension of soil moisture over a wide moisture range, Soil Sci., 43, 277–284, doi:10.1097/00010694-193704000-00004, 1937. 2810, 2813

SED
7, 2807–2831, 2015

Hall, S.: Discrete and continuum analysis of localised deformation in sand using X-ray μCT and volumetric digital image correlation, Géotechnique, 60, 315–322, doi:10.1680/geot.2010.60.5.315, 2010. 2809
Hapca, S. M., Wang, Z. X., Otten, W., Wilson, C., and Baveye, P. C.: Automated statistical method to align 2-D chemical maps with 3-D X-ray computed micro-tomographic images of soils, Geoderma, 164, 146–154, doi:10.1016/j.geoderma.2011.05.018, 2011. 2811
Ibanez, L., Schroeder, W., Ng, L., and Cates, J.: The ITK Software Guide, 2nd edn., Kitware Inc., Clifton Park, NY, USA, 787 pp., 2005. 2814
Jawahar, C., Biswas, P., and Ray, A.: Investigations on fuzzy thresholding based on fuzzy clustering, Pattern Recogn., 30, 1605–1613, doi:10.1016/S0031-3203(97)00004-6, 1997. 2815
Jégou, D., Brunotte, J., Rogasik, H., Capowiez, Y., Diestel, H., Schrader, S., and Cluzeau, D.: Impact of soil compaction on earthworm burrow systems using X-ray computed tomography: preliminary study, Eur. J. Soil Biol., 38, 329–336, doi:10.1016/S1164-5563(02)01148-2, 2002. 2809
Kaestner, A., Lehmann, E., and Stampanoni, M.: Imaging and image processing in porous media research, Adv. Water Resour., 31, 1174–1187, doi:10.1016/j.advwatres.2008.01.022, 2008. 2809
Ketcham, R. and Carlson, W.: Acquisition, optimization and interpretation of X-ray computed tomographic imagery: applications to the geosciences, Comput. Geosci., 27, 381–400, 2001. 2808
Khanzode, R. M., Vanapalli, S. K., and Fredlund, D. G.: Measurement of soil-water characteristic curves for fine-grained soils using a small-scale centrifuge, Can. Geotech. J., 39, 1209–1217, doi:10.1139/t02-060, 2002. 2810
Klein, S., Staring, M., Murphy, K., Viergever, M., and Pluim, J.: elastix: a toolbox for intensity-based medical image registration, IEEE T. Med. Imaging, 29, 196–205, doi:10.1109/TMI.2009.2035616, 2010. 2811, 2814, 2815
Latham, S., Varslot, T., and Sheppard, A.: Image registration: enhancing and calibrating X-ray micro-CT imaging, in: Proceedings of the Society of Core Analysis, Abu Dhabi, UAE, October 2008, SCA2008-35, 2008. 2811, 2812
Leij, F., Ghezzehei, T., and Or, D.: Analytical models for soil pore-size distribution after tillage, Soil Sci. Soc. Am. J., 66, 1104–1114, 2002. 2820

SED
7, 2807–2831, 2015

Lenoir, N., Bornert, M., Desrues, J., Bésuelle, P., and Viggiani, G.: Volumetric digital image correlation applied to X-ray microtomography images from triaxial compression tests on argillaceous rock, Strain, 43, 193–205, doi:10.1111/j.1475-1305.2007.00348.x, 2007. 2809

Mattes, D., Haynor, D. R., Vesselle, H., Lewellyn, T. K., and Eubank, W.: Nonrigid multimodality image registration, SPIE Proceedings, vol. 4322, Medical Imaging 2001: Image Processing, San Diego, CA, USA, 17 February 2001, 1609–1620, doi:10.1117/12.431046, 2001. 2811, 2815

Oden, S.: An integral method for the determination of moisture retention curves by centrifugation, Grundfoerbaettring, 27, 137–143, 1975. 2810

Peters, A. and Durner, W.: Simplified evaporation method for determining soil hydraulic properties, J. Hydrol., 356, 147–162, doi:10.1016/j.jhydrol.2008.04.016, 2008. 2810

Peth, S., Nellesen, J., Fischer, G., and Horn, R.: Non-invasive 3-D analysis of local soil deformation under mechanical and hydraulic stresses by μCT and digital image correlation, Soil Till. Res., 111, 3–18, 2010. 2809

Reatto, A., Da Silva, E. M., Bruand, A., Martins, E. S., and Lima, J. E. F. W.: Validity of the centrifuge method for determining the water retention properties of tropical soils, Soil Sci. Soc. Am. J., 72, 1547–1553, doi:10.2136/sssaj2007.0355N, 2008. 2810

Russell, M. and Richards, L.: The determination of soil moisture energy relations by centrifugation, Soil Sci. Soc. Am. J., 3, 65–69, 1939. 2810, 2813

Schlüter, S., Weller, U., and Vogel, H.-J.: Soil-structure development including seasonal dynamics in a long-term fertilization experiment, J. Plant Nutr. Soil Sc., 174, 395–403, doi:10.1002/jpln.201000103, 2011. 2809

Schlüter, S., Sheppard, A., Brown, K., and Wildenschild, D.: Image processing of multiphase images obtained via X-ray microtomography: a review, Water Resour. Res., 50, 3615–3639, doi:10.1002/2014WR015256, 2014. 2809, 2815, 2816

Šimůnek, J. and Nimmo, J. R.: Estimating soil hydraulic parameters from transient flow experiments in a centrifuge using parameter optimization technique, Water Resour. Res., 41, w04015, doi:10.1029/2004WR003379, 2005. 2810

Simunek, J., van Genuchten, M. T., and Wendroth, O.: Parameter estimation analysis of the evaporation method for determining soil hydraulic properties, Soil Sci. Soc. Am. J., 62, 894–905, doi:10.2136/sssaj1998.03615995006200040007x, 1998. 2810

Son, A., Medina-Cetina, Z., and Rechenmacher, A.: Local Deformation Analysis of a Sand Specimen Using 3-D Digital Image Correlation for the Calibration of a Simple Elasto-Plastic

SED
7, 2807–2831, 2015

Model, chap. 235, Geotechnical Special Publication, ASCE, Reston, VA, USA, 2292–2301, doi:10.1061/9780784412121.235, 2012. 2809
Terzaghi, K., Peck, R. B., and Mesri, G.: Soil Mechanics in Engineering Practice, John Wiley and Sons, New York, NY, USA, 1996. 2809
Tristán-Vega, A., García-Pérez, V., Aja-Fernández, S., and Westin, C.-F.: Efficient and robust nonlocal means denoising of MR data based on salient features matching, Comput. Meth. Prog. Bio., 105, 131–144, doi:10.1016/j.cmpb.2011.07.014, 2012. 2815
Van Dam, J., Stricker, J., and Droogers, P.: Inverse method to determine soil hydraulic functions from multistep outflow experiments, Soil Sci. Soc. Am. J., 58, 647–652, doi:10.2136/sssaj1994.03615995005800030002x, 1994. 2810
Van den Berg, E., Perfect, E., Tu, C., Knappett, P., Leao, T., and Donat, R.: Unsaturated hydraulic conductivity measurements with centrifuges: a review, Vadose Zone J., 8, 531–547, doi:10.2136/vzj2008.0119, 2009. 2810
van Genuchten, M.: A closed-form equation for predicting the hydraulic conductivity of unsaturated soils, Soil Sci. Soc. Am. J., 44, 892–898, 1980. 2816
Vogel, H.-J. and Ippisch, O.: Estimation of a critical spatial discretization limit for solving Richards' equation at large scales, Vadose Zone J., 7, 112–114, 2008. 2810
Vogel, H.-J., Weller, U., and Schlüter, S.: Quantification of soil structure based on Minkowski functions, Comput. Geosci., 36, 1236–1245, doi:10.1016/j.cageo.2010.03.007, 2010. 2809, 2816
Wedler, W. and Boguslawski, E.: Zur Methodik der pF-Wert-Bestimmung mit der Zentrifuge, Zeitschrift für Pflanzenernährung, Düngung, Bodenkunde, 109, 249–260, 1965. 2810, 2819
White, D. J.: Soil deformation measurement using particle image velocimetry (PIV) and photogrammetry, Géotechnique, 53, 619–631(12), doi:10.1680/geot.2003.53.7.619, 2003. 2809
Wildenschild, D. and Sheppard, A. P.: X-ray imaging and analysis techniques for quantifying pore-scale structure and processes in subsurface porous medium systems, Adv. Water Resour., 51, 217–246, doi:10.1016/j.advwatres.2012.07.018, 35th Year Anniversary Issue, 2013. 2808

SED
7, 2807–2831, 2015

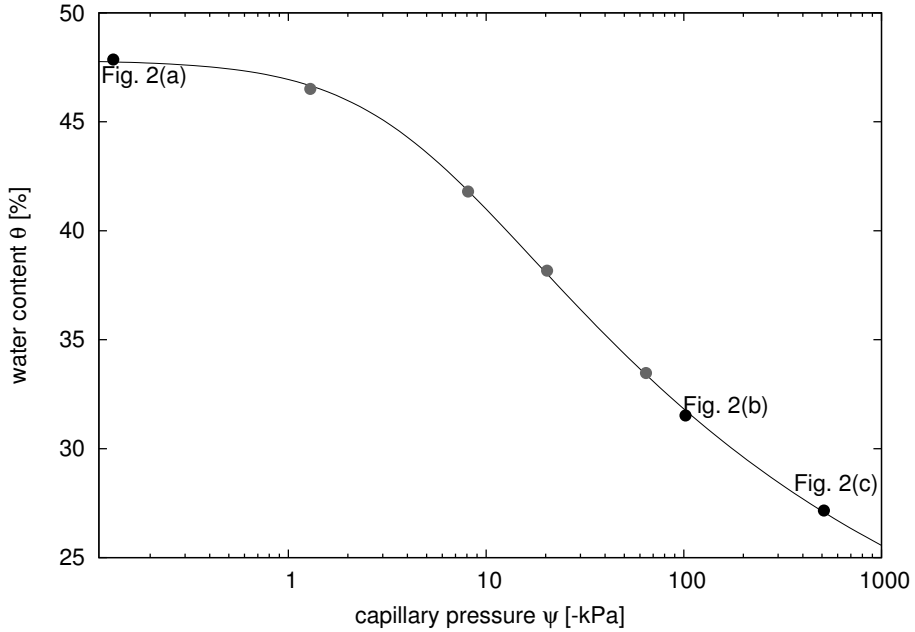

Figure 1. Water content as function of capillary pressure. The line respresents a fit of a van Genuchten function (R^2 = 0.999) with the following parameters: α = 0.23 kPa^{-1}, n = 1.22, θ_s = 0.47, θ_r = 0.16. The black circles represent the capillary pressures for which X-ray microtomography scans were acquired.

SED
7, 2807–2831, 2015

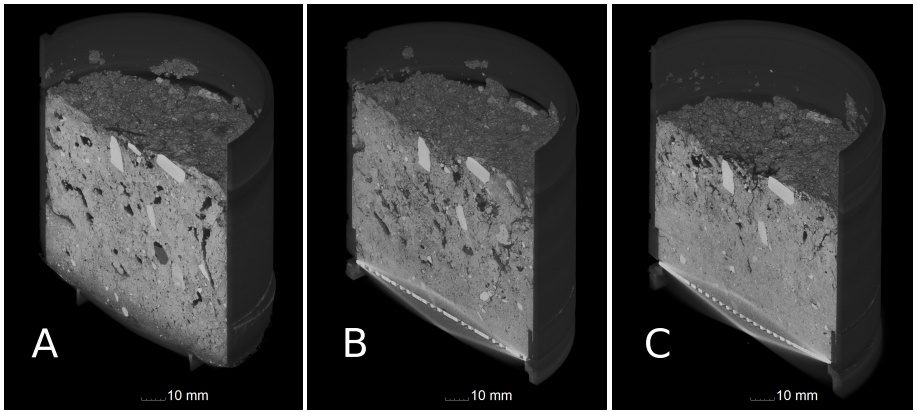

Figure 2. Soil structure obtained with X-ray microtomography **(a)** at full water saturation (ψ = 0 kPa) and **(b)** at ψ = −100 kPa and **(c)** at ψ = −500 kPa.

SED
7, 2807–2831, 2015

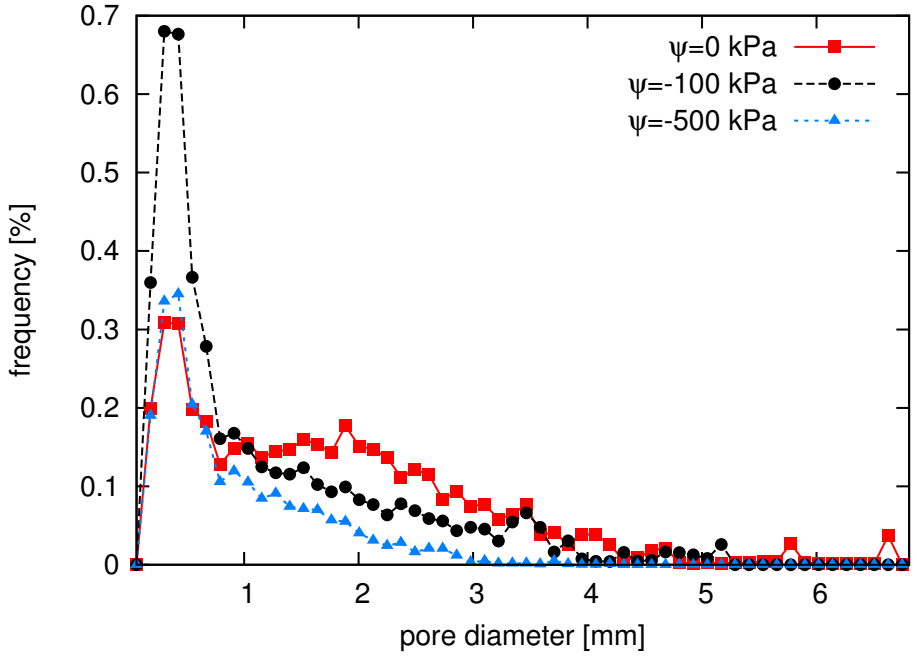

Figure 3. Pore size distribution in the soil at three different capillary pressures.

SED
7, 2807–2831, 2015

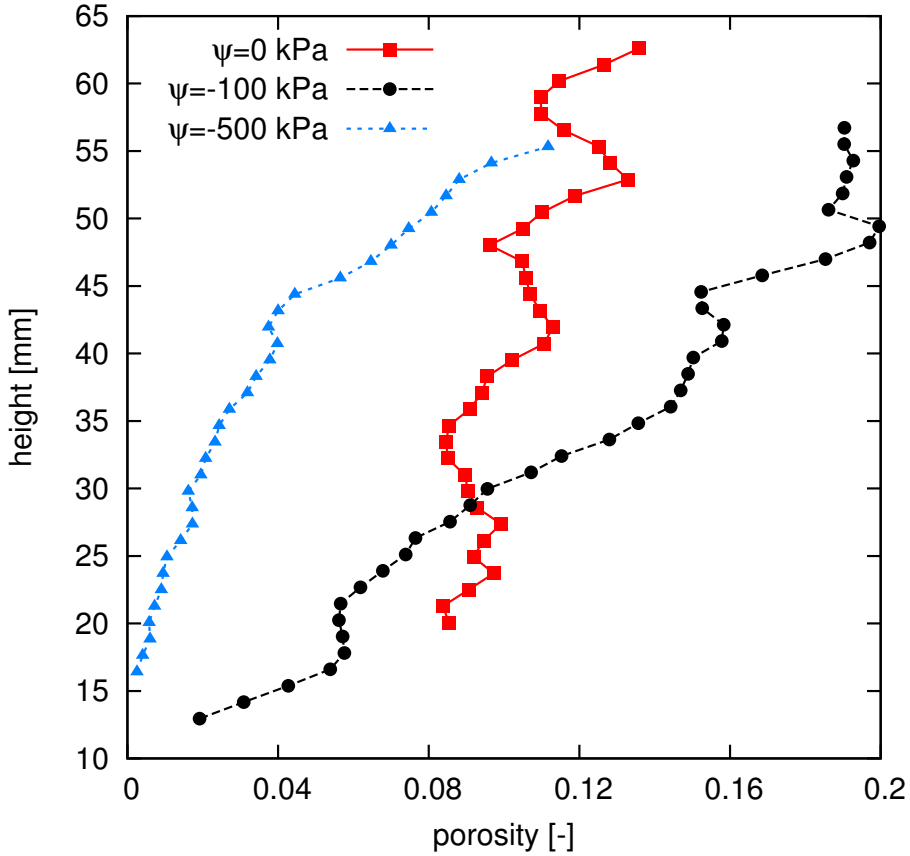

Figure 4. Depth profile of porosity at three different capillary pressures. All images cover slightly different field of views and are normalized to a reference height at the bottom of the sample.

SED
7, 2807–2831, 2015

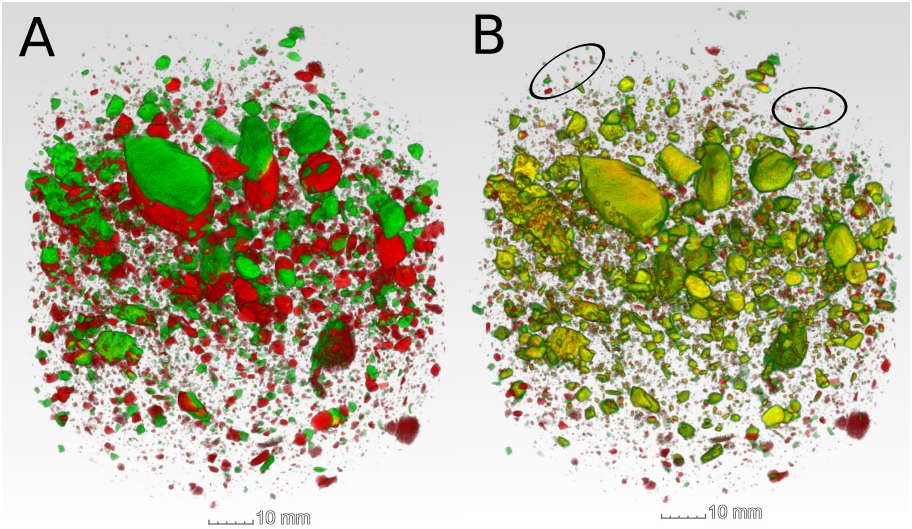

Figure 5. The spatial alignment of rocks between the saturated soil (green) and the soil at $\psi = -500$ kPa (red) before **(a)** and after **(b)** elastic registration. Note that the co-occurence of rocks results in a composite, yellowish color. The black frames highlight the mismatch for small rocks.

SED
7, 2807–2831, 2015

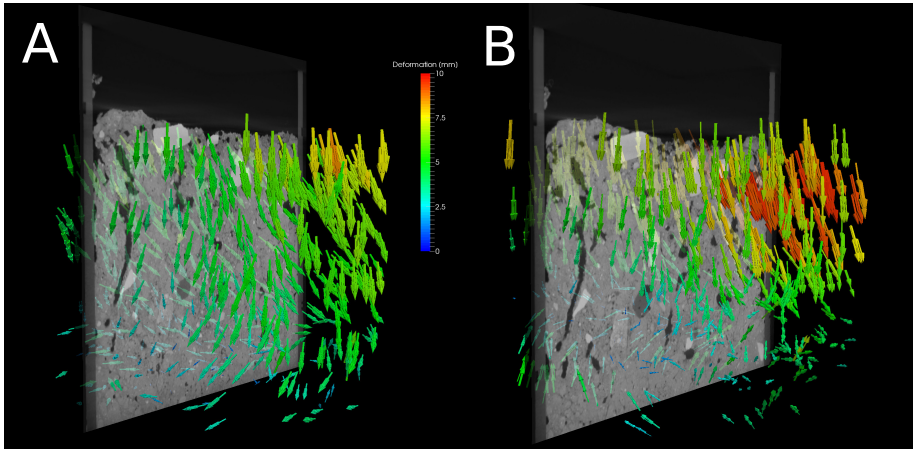

Figure 6. Displacement vector field for the soil at a capillary pressure of **(a)** $\psi = -100$ kPa and **(b)** $\psi = -500$ kPa. Only a small percentage of all vectors is displayed to improve visibility. The vector length correponds to the physical displacement. The 2-D section of the undisturbed soil is for orientation.

SED
7, 2807–2831, 2015